Three-dimensional vision based on a combination of gray-code and phase-shift light projection: analysis and compensation of the systematic errors

Giovanna Sansoni, Matteo Carocci, and Roberto Rodella

A combination of phase-shift with gray-code light projection into a three-dimensional vision system based on the projection of structured light is presented.   The gray-code method is exploited to detect without ambiguity even marked surface discontinuities, whereas the phase-shift technique allows the measurement of fine surface details.   The system shows excellent linearity.   An overall mean value of the measurement error equal to 40 μm, with a variability of approximately ±35 μm, corresponding to 0.06% of full scale, has been estimated.   The implementation of the technique is discussed, the analysis of the systematic errors is presented in detail, and the calibration procedure designed to determine the optimal setting of the measurement parameters is illustrated.   © 1999 Optical Society of America

OCIS codes: 120.0120, 120.2830, 120.3930, 150.0150, 150.6910.

1.   Introduction

The evaluation of three-dimensional (3D) shapes by means of optical sensors has an increasing importance in a number of applications because of the intrinsic noncontact nature of the measurement and the possibility of reducing the measurement time with respect to contact probes.   Typical applications in the industrial field are production quality control, both in the microrange and in the macrorange,[1] the digitization of free-shape surfaces in the reverse engineering process,[2] and a number of 3D computer vision problems.[3]   More recently, they have been successfully used in other fields, such as archeology, for measuring and preserving cultural heritage and in entertainment and 3D virtual reality frameworks.[4]

A number of publications now exist on the optical techniques developed for 3D measurement, both of the passive and the active nature.   In passive methods, no controlled source of light is necessary: Surface reflectance, stereo disparity, and camera motion are examples of techniques based on this passive ap-

proach.   The main drawback is represented by the high computational effort needed to get depth information.[5]   In active methods, use of a pattern of radiation simplifies the problem of depth measurement.   Interferometric and moiré techniques achieve very accurate measurements over small depth ranges,[6] time-of-flight methods are suitable for medium and long distances,[7] and triangulation-based methods match the short-distance interval: Within this frame, the systems based on the scanning of coherent light are widely used,[8] as well as whole-field profilometers, based on the projection of structured light.   A number of pattern projection schemes belong to this last category and differ from each other in the coding used to express the light directions.[9–13]

The research activity reported in this paper deals with the implementation of a technique that combines two methods for the projection and the demodulation of bidimensional patterns of light, known as the gray-code and the phase-shift methods.   The resulting technique, (hereafter called GCPS) has been integrated into a prototype for 3D vision developed at our laboratory to achieve a system that performs at optimal accuracy and speed over a wide typology of objects.

The gray-code technique allows the unique description of 2^n different directions of projection by means of the well-known one-distance gray code.   The number of the directions of projection that can be unequivocally defined equals the number of the code words: thus, the larger this number, the wider the nonam-

The authors are with the Instituto Nazionale Fisica della Materia and the Dipartimento di Elettronica per l'Automazione, Università degli Studi di Brescia, Via Branze 38, I-25123 Brescia, Italy.   G. Sansoni's e-mail address is sansoni@bsing.ing.unibs.it.

biguity height range. On the other hand, as each projection direction is associated with a code word, but not further decomposed, the measurement resolution is rather low.[11]

With the phase-shift approach, the directions of projection are coded by phase values: Because the phase is continuously distributed within its range of nonambiguity, a theoretically infinite height resolution can be obtained, actually limited only by the errors that are due to gray-level quantization and noise. On the other hand, the range of nonambiguity is limited to the interval 0–2π, and this fact strongly reduces the height range.[12]

The combination of gray code and phase shift in GCPS has been proposed by several authors to exploit the positive features of each method and compensate for their drawbacks.[13] In principle, the latter is used to increase the information given by the former by adding a fractional contribution to the code words that identify each direction of projection. Consequently the measurement performance is strongly improved as to the resolution and the range of the measurement.

As part of the work performed, we revisited the theory of GCPS to compensate for the influence of the crossed-optical-axes geometry of the system, which determines a spatial modulation of the fringes even in the absence of the target.[14] The resulting triangulation procedure is given in detail in this paper.

Moreover, we present the analysis of the systematic measuring errors and the calibration procedure designed to determine the estimates of the measurement parameters at optimal accuracy and speed. The set of experiments carried out to evaluate the system performance is also reported. In this context, we thought it important to derive the in–out characteristic curves of the system that correspond to a considerable number of measuring points in the work volume and to characterize them in terms of linearity.

Section 2 describes the projection technique and the triangulation procedure, Section 3 reports the analysis of the systematic errors introduced by an inaccuracy in the determination of the parameters involved in the measurement, Section 4 is devoted to the description of the calibration procedure, and Section 5 shows the experimental results.

2. Description of the Technique

The basic outline of the technique is summarized here with the aid of Fig. 1. Points P and C represent the exit and the entrance pupils of the projection and the imaging optics, respectively, d is the distance between them, and L is the distance from plane R. The coordinate system at the projection sensor plane (PSP) is (X^p, Y^p, Z^p) and that of the image sensor plane (ISP) is (X^c, Y^c, Z^c): The origins are at points P and C, respectively. Axes Z^p and Z^c coincide with the optical axes of the projection and the imaging devices: Z^c is perpendicular to reference R, and Z^p is at an angle with respect to Z^c. The depth information is defined along the Z coordinate in the reference
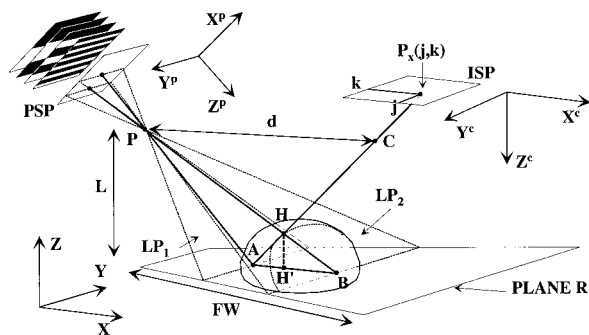

Fig. 1. Optical geometry of the system.

system (X, Y, Z). The discrete coordinates at the ISP are j and k, corresponding respectively to X^c and Y^c. FW is the width of the field of view along the X coordinate.

Because the fringes formed at the PSP are parallel to Y^p, when the X^p coordinate varies, different light planes can be identified: As an example, Fig. 1 shows two light planes, denoted by LP_1 and LP_2, defined in correspondence to two different values of coordinate X^p. In the figure, light ray $\overline{PA}$ on LP_1 is also depicted: It intersects plane R at point A and is imaged by pixel $P_x(j, k)$ at the ISP. Axes Y^p, Y^c, and Y are all parallel to each other: Thus the measuring procedure does not involve them and in the following they are not considered.

GCPS is based on two different steps. The first one is aimed at coding the light planes from the projector; the second step exploits light codings to evaluate the height.

A. Light Coding Based on the Combination of Gray-Code and Phase-Shift Projection

The coding procedure that combines the gray-code method with the phase-shift method is based on the projection, at $n = 11$ subsequent instants, of n black and white fringe patterns: The first seven patterns of the sequence, denoted by GC_0, GC_1, ..., GC_6, are formed in such a way that their projection corresponds to the formation of a gray code of 7 bits. As an example, the projection of patterns GC_0, GC_1, GC_2, and GC_3 on plane R corresponds to the formation of the gray code shown in Table 1. Rows r_0, r_1, r_2, and r_3 of the table codify word bits from the most-significant to the least-significant one and can be interpreted as the binary representation of patterns GC_0, GC_1, GC_2, and GC_3 along the X direction, provided that black fringes are assigned to the logic value 0 and white fringes are assigned to the logic value 1. Columns c_0, c_1, ..., c_{15} are the code words.

Each pattern is recorded in sequence by the video camera, and a suitable thresholding algorithm associates either the logic value 0 or 1 with the gray level of each CCD pixel. Figure 2 gives a pictorial representation of how the gray-code word defined by the bit sequence 0111 is determined in correspondence to the element of position (j, k) on the ISP ($n = 4$ is still

Table 1. Gray-Code Sequence for $n = 4$

Word Bits	c_0	c_1	c_2	c_3	c_4	c_5	c_6	c_7	c_8	c_9	c_{10}	c_{11}	c_{12}	c_{13}	c_{14}	c_{15}
r_0	0	0	0	0	0	0	0	0	1	1	1	1	1	1	1	1
r_1	0	0	0	0	1	1	1	1	1	1	1	1	0	0	0	0
r_2	0	0	1	1	1	1	0	0	0	0	1	1	1	1	0	0
r_3	0	1	1	0	0	1	1	0	0	1	1	0	0	1	1	0

considered). This word codes the light ray seen by pixel $P_x(j, k)$ in Fig. 1, as well as all the rays on light plane LP_1. The number of light planes unequivocally defined by this method equals the number of the code words: thus, the larger this number, the wider the nonambiguity range of the measurement. In our system, 2^7 words, 7 bits deep, can be defined; in the following they are referred to as $\hat{l}$. The gray-code word describing the light ray seen by the video camera at $P_x(j, k)$ on the ISP is denoted as $\hat{l}(j, k)$.

The last four patterns are obtained as follows: The pattern of the gray-code sequence corresponding to the eighth bit is generated and then spatially shifted by a fraction $p/4$ of its spatial period p. The resulting patterns, called PS_0, PS_1, PS_2, and PS_3, are acquired and digitally smoothed in order to obtain fringes of the sinusoidal profile.[15] The intensity fields $I_i(j, k)$ acquired that correspond to each shift ($i = 0, 1, 2, 3$) can be expressed as follows:

$$I_i(j, k) = A(j, k) + \frac{B(j, k)}{2} \cos\left[\Phi(j, k) - i\frac{\pi}{2}\right]. \quad (1)$$

In Eq. (1), $A(j, k)$ and $B(j, k)$ account for the average brightness and the fringes' contrast, respectively, and $\Phi(j, k)$ represents the phase term. It is evaluated by means of the following, well-known relationship[14]:

$$\Phi(j, k) = \tan^{-1}\frac{I_1(j, k) - I_3(j, k)}{I_0(j, k) - I_2(j, k)} \quad (2)$$

In Eq. (2), $\Phi(j, k)$ is the phase coding describing the light ray seen by the video camera at $P_x(j, k)$ on the ISP. This description is not unequivocal, as the range of nonambiguity is limited to the interval $0-2\pi$; however, it yields high resolution, as the phase
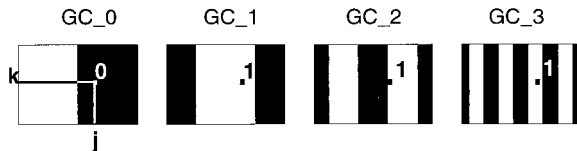
is continuously distributed within its range of nonambiguity.

The integer coding obtained from the gray-code sequence and the phase coding from the phase-shift approach are then combined as follows:

$$l(j, k) = \hat{l}(j, k) + \frac{2}{\pi}[\Phi(j, k) + \Delta\Phi(j, k)]. \quad (3)$$

In Eq. (3), $l(j, k)$ is a real number and denotes the complete coding, and $\Delta\Phi(j, k)$ represents a phase-correction term, experimentally evaluated, as shown in Table 2. The expression of light directions by means of real numbers $l(j, k)$ in Eq. (3) intrinsically yields the extended measurement ranges typical of the gray-code method, as well as high resolution, because of the fractional part obtained from phase shift.

B. Depth Evaluation by Means of Triangulation

Figure 1 shows the triangulation principle: For simplicity, it is applied to the measurement of height $z_H = \overline{HH'}$, even though it holds for each point in the coded area on reference R. Two different light rays are viewed along the same direction of acquisition ($\overline{AC}$ in the figure): These are ray $\overline{PA}$ and ray $\overline{PB}$. They lay on light planes LP_1 and LP_2, respectively, and are imaged at pixel $P_x(j, k)$ on the ISP, the former in the absence of the object, the latter when the object is placed on reference R. With the coding of light planes LP_1 and LP_2 denoted by l_{PA} and l_{PB}, it will be $l(j, k) = l_{PA}$ in the absence of the object and $l(j, k) = l_{PB}$ in the presence of the object. Height z_H is evaluated by considering that triangles $A\hat{H}B$ and $P\hat{H}C$ are similar and that the following equation holds:

$$z_H = \frac{L\overline{AB}}{d + \overline{AB}}. \quad (4)$$

In Eq. (4), L and d are defined by the geometry of the system, and $\overline{AB}$ is the base of triangle $A\hat{H}B$, representing the distance between rays $\overline{PA}$ and $\overline{PB}$. Thus a preliminary step to the use of Eq. (4) is the evaluation of $\overline{AB}$. To this aim, we developed a specific procedure that transforms each light coding into the corresponding abscissa along the X coordinate directly at reference R. This means, for the example

Fig. 2. Example of the pattern sequence that combines gray-code and phase-shift projection.

Table 2. Evaluation of the Correction Term $\Delta\Phi(j, k)$

$\Delta\Phi(j, k)$	$\Phi(j, k) \in [-\pi, -\pi/2]$	$\Phi(j, k) \in [-\pi/2, 0]$	$\Phi(j, k) \in [0, \pi/2]$	$\Phi(j, k) \in [\pi/2, \pi]$
$\hat{l}(j, k)\bmod 4 \equiv 0$	$3\pi/2$	$-\pi/2$	$-\pi/2$	$-\pi/2$
$\hat{l}(j, k)\bmod 4 \equiv 3$	π	π	π	$-\pi$

Fig. 3. Model of the system geometry used to derive the mapping equation.

in Fig. 1, that light codings l_{PA} and l_{PB} are mapped into the values of the X coordinate of points A and B (i.e., x_A and x_B), and shift $\overline{AB}$ is computed as

$$\overline{AB} = x_B - x_A. \qquad (5)$$

The mapping equation, shown here for the evaluation of x_B, has the form

$$x_B = \overline{PQ} \tan(\gamma + \delta_x) = L \tan(\gamma + \delta_x). \qquad (6)$$

Equation (6) is derived from the geometric model shown in Fig. 3. In this figure, segments $\overline{PS}$ and $\overline{PT}$ represent the first and the last directions of projection seen by the video camera, respectively, and define the length of field of view FW; segment $\overline{ST'}$ represents a plane parallel to the PSP at angle α with respect to plane R and intersecting it at point S. Angle γ is the angle between ray $\overline{PS}$ and line $\overline{PQ}$, perpendicular to reference R. It is expressed by

$$\gamma = \tan^{-1}\left(\dfrac{d - \dfrac{FW}{2}}{L}\right). \qquad (7)$$

δ_x represents the angle between ray $\overline{PS}$ and ray $\overline{PB}$. It is evaluated by application of the law of sines to triangle $S\hat{B}'P$:

$$\dfrac{\overline{SB'}}{\sin \delta_x} = \dfrac{\overline{SP}}{\sin \theta_x}. \qquad (8)$$

In Eq. (8), θ_x is the angle between $\overline{ST'}$ and $\overline{PB}$, and $\overline{SB'}$ represents the distance from point S of the intersection point between $\overline{ST'}$ and ray $\overline{PB}$. Considering that $\theta_x = (\pi/2) - \gamma - \delta_x + \alpha$ and solving Eq. (8) with respect to δ_x, we obtain

$$\delta_x = \tan^{-1}\left[\dfrac{\overline{SB'} \cos(\gamma - \alpha)}{\overline{SP} + \overline{SB'} \sin(\gamma - \alpha)}\right]. \qquad (9)$$

Because segment $\overline{ST'}$ is parallel to the PSP, distance $\overline{SB'}$ can be expressed as a linear function of l_{PB}:

$$\overline{SB'} = \dfrac{l_{PB}}{nlp} \overline{ST'}, \qquad (10)$$

where the parameter nlp represents the total number of light codings that fall within the field of view at plane R. The length of segment $\overline{ST'}$ in Eq. (10) is evaluated with Eq. (8) for the case in which B' is coincident with T':

$$\overline{ST'} = \dfrac{\sin \delta_{\mathrm{tot}}}{\sin \theta_{\mathrm{tot}}} \overline{SP} = \dfrac{\sin \delta_{\mathrm{tot}}}{\sin \theta_{\mathrm{tot}}} \dfrac{L}{\cos(\gamma)}. \qquad (11)$$

Angles δ_{tot} and θ_{tot} can be respectively expressed as

$$\delta_{\mathrm{tot}} = \tan^{-1}\left[\dfrac{L \tan(\gamma) + FW}{L}\right] - \gamma, \qquad (12)$$

$$\theta_{\mathrm{tot}} = \dfrac{\pi}{2} + \alpha - \tan^{-1}\left[\dfrac{L \tan(\gamma) + FW}{L}\right]. \qquad (13)$$

The combination of Eqs. (8)–(13) into Eq. (6) results in the following expression for x_B:

$$x_B = L\left(\tan\left\{\gamma + \tan^{-1}\left[\dfrac{C_l l_{PB} \cos(\gamma - \alpha)}{1 + C_l l_{PB} \sin(\gamma - \alpha)}\right]\right\}\right). \qquad (14)$$

In Eq. (14), C_1 is a constant, defined as

$$C_1 = \dfrac{\sin(\delta_{\mathrm{tot}})}{(nlp)\sin(\theta_{\mathrm{tot}})}. \qquad (15)$$

Equation (14) expresses the abscissa x_B as a nonlinear function of l_{PB}, L, d, FW, and α. This is a direct consequence of the crossed-optical-axes geometry of the system: In fact, points P and C are at finite distance L, and the fringes projected on reference R show increasing period p_R along axis X. A linear mapping, such as that presented in Ref. 13, can be successfully applied only if p_R can be considered constant on reference R: in fact, in this case, $\overline{AB}$ linearly depends on the difference $[l_{PB} - l_{PA}]$, on FW, and on period p_R. However, this hypothesis holds as far as distance L is sufficiently large and angle α is sufficiently small to limit the dependence of p_R on X. In contrast, for the geometric setups characterized by reduced values for L and increased values for α, any attempt at evaluating $\overline{AB}$ by use of constant p_R inherently yields an error in the estimation of the height. The use of Eq. (14) overcomes this problem because it precisely models the relation between the position along X of the points where the projected light rays impinge on reference R and the corresponding light codings. This derivation is performed punctually and is intrinsically insensitive to any variation of p_R.

The extension of the presented measuring principle to any point over the illuminated area is carried out as follows: (1) the complete sequence of patterns from GC_0 to PS_3 is projected and elaborated in the two situations of absence and of presence of the object, yielding two matrices respectively called REF for the reference and OBJ for the object. A one-to-one correspondence is established between the pixels of the CCD and the elements of each matrix: For the example in Fig. 1, it results in REF(j, k) = l_{PA} and OBJ(j, k) = l_{PB}. These matrices are then trans-

formed, by means of Eq. (14), into matrices $\mathbf{x}_{\text{REF}}$ and $\mathbf{x}_{\text{OBJ}}$, which store the corresponding abscissa values. Finally, the difference between them is calculated when Eq. (5) is applied to each element of $\mathbf{x}_{\text{REF}}$ and $\mathbf{x}_{\text{OBJ}}$:

$$
\begin{aligned}
D_R(j, k) &= x_{\text{OBJ}}(j, k) - x_{\text{REF}}(j, k) \\
&= L\left(\tan\left\{ \gamma + \tan^{-1}\left[\frac{C_1\text{OBJ}(j, k)\cos(\gamma - \alpha)}{1 + C_1\text{OBJ}(j, k)\sin(\gamma - \alpha)} \right] \right\} \right. \\
&\quad \left. - \tan\left\{ \gamma + \tan^{-1}\left[\frac{C_1\text{REF}(j, k)\cos(\gamma - \alpha)}{1 + C_1\text{REF}(j, k)\sin(\gamma - \alpha)} \right] \right\} \right)
\end{aligned}
$$

$$(16)$$

where $\mathbf{D}_R$ is the difference matrix. Equation (4) can be rewritten as

$$
z(j, k) = \frac{L D_R(j, k)}{d + D_R(j, k)} \tag{17}
$$

where $z(j, k)$ is the element of matrix $\mathbf{z}$, storing the measured height in millimeters.

3. Analysis of the Systematic Errors

An analysis of the systematic errors introduced into the measured height by inaccuracies in the determination of the model parameters has been performed to evaluate how critical these are for the accuracy of the measurement. This analysis has been limited to parameters L, d, and α, as FW can be easily evaluated with small uncertainty during the setup of the measurement by the exploitation of suitable two-dimensional processing for the determination of the scale factor from pixels to millimeters at the reference. In contrast, the accurate determination of L, d, and α is not possible because of the difficulty of precisely measuring the position of the pupils of the projector and of the video camera and because the orientation of the LCD within the projector is unknown.

In the following, L_e, d_e, and α_e represent the estimates of L, d, and α, and $\Delta L/L = (L_e - L)/L$, $\Delta d/d = (d_e - d)/d$, and $\Delta\alpha/\alpha = (\alpha_e - \alpha)/\alpha$ express the inaccuracies of each parameter. The error $\Delta z(j, k)/z(j, k)$ is expressed as the sum of three terms:

$$
\frac{\Delta z(j, k)}{z(j, k)} = \frac{\Delta z_L(j, k) + \Delta z_d(j, k) + \Delta z_\alpha(j, k)}{z(j, k)}, \tag{18}
$$

where $\Delta z_L(j, k)$, $\Delta z_d(j, k)$, and $\Delta z_\alpha(j, k)$ account for the influence of inaccuracies $\Delta L/L$, $\Delta d/d$, and $\Delta\alpha/\alpha$, respectively.

A. Influence of Parameter L

Term $\Delta z_L(j, k)$ is derived as the difference between the height calculated by Eq. (17) that corresponds to values L_e and L:

$$
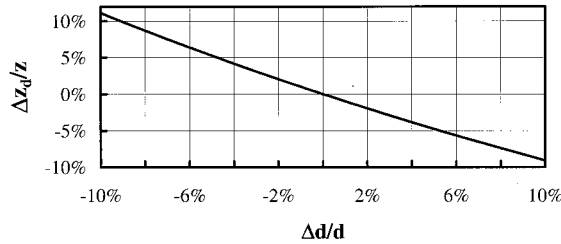\Delta z_L(j, k) = \frac{L_e D_R(j, k)}{d + D_R(j, k)} - \frac{L D_R(j, k)}{d + D_R(j, k)}. \tag{19}
$$
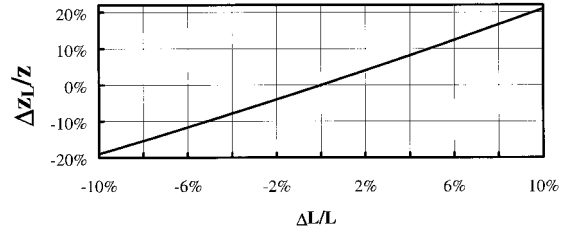
Fig. 4. Plot of the systematic error $\Delta z_L/z$ as a function of $\Delta L/L$.

From Eq. (16), $D_R(j, k)$ can be expressed as

$$
D_R(j, k) = L C_2, \tag{20}
$$

where C_2 is

$$
\begin{aligned}
C_2 &= \tan\left\{ \gamma - \tan^{-1}\left[\frac{C_1\text{OBJ}(j, k)\cos(\gamma - \alpha)}{1 + C_1\text{OBJ}(j, k)\sin(\gamma - \alpha)} \right] \right\} \\
&\quad - \tan\left\{ \gamma - \tan^{-1}\left[\frac{C_1\text{REF}(j, k)\cos(\gamma - \alpha)}{1 + C_1\text{REF}(j, k)\sin(\gamma - \alpha)} \right] \right\}.
\end{aligned}
$$

$$(21)$$

It has been experimentally proven that C_2 has a negligible dependence on L and, for practical purposes, can be considered constant. When Eqs. (19) and (20) are combined, error $\Delta z_L(j, k)/z(j, k)$ results:

$$
\frac{\Delta z_L(j, k)}{z(j, k)} = \frac{\dfrac{C_2 L_e^2}{d + C_2 L_e}}{\dfrac{C_2 L^2}{d + C_2 L}} - 1. \tag{22}
$$

Considering that parameter d is usually much larger than the products $C_2 L_e$ and $C_2 L$, Eq. (22) becomes

$$
\frac{\Delta z_L(j, k)}{z(j, k)} = \frac{L_e^2}{L^2} - 1 = \frac{(L + \Delta L)^2 - L^2}{L^2} = 2\frac{\Delta L}{L} + \left(\frac{\Delta L}{L}\right)^2. \tag{23}
$$

Equation (23) shows that error $\Delta z_L(j, k)/z(j, k)$ is an almost linear function of $\Delta L/L$. This dependence is shown in Fig. 4, where $\Delta L/L$ is varied within the interval -10%–10%: The quadratic term is negligible, and the sensitivity coefficient is equal to 2.

B. Influence of Parameter d

The term $\Delta z_d(j, k)$ is derived as the difference between the height calculated by Eq. (17) that corresponds to values d_e and d:

$$
\Delta z_d(j, k) = \frac{L D_R(j, k)}{d_e + D_R(j, k)} - \frac{L D_R(j, k)}{d + D_R(j, k)}. \tag{24}
$$

Fig. 5. Plot of the systematic error $\Delta z_d/z$ as a function of $\Delta d/d$.

Fig. 6. Plot of the systematic error $\Delta z_\alpha/z$ as a function of $\Delta \alpha/\alpha$.

Thus $\Delta z_d(j, k)/z(j, k)$ results:

$$
\frac{\Delta z_d(j, k)}{z(j, k)} = \frac{\dfrac{LD_R(j, k)}{d_e + D_R(j, k)}}{\dfrac{LD_R(j, k)}{d + D_R(j, k)}} - 1
$$

$$
= \frac{d - d_e}{d_e + D_R(j, k)}
$$

$$
= -\frac{\Delta d}{d} \frac{1}{1 + \dfrac{\Delta d}{d} + \dfrac{D_R(j, k)}{d}}. \qquad (25)
$$

Equation (25) expresses $\Delta z_d(j, k)/z(j, k)$ as a hyperbolic function of $\Delta d/d$; however, for small values of $\Delta d/d$ this function is almost linear, as shown in Fig. 5. Here, the sensitivity coefficient

$$
-\frac{1}{1 + \dfrac{D_R(j, k)}{d}}
$$

is very close to -1.

C. Influence of Parameter α

The analytical derivation of the dependence of $\Delta z_\alpha(j, k)$ on α is very difficult to achieve with the above method, mainly because, in Eq. (17), $D_R(j, k)$ is a nonlinear function of α. Thus this dependence is studied with a simulation-based approach, consisting of the following steps: (1) matrix $\mathbf{D}_R$ is evaluated by means of Eq. (17) for known values of L and d and for constant height; (2) supposing that $\mathbf{x}_{\mathrm{REF}}$ is constant, matrix $\mathbf{x}_{\mathrm{OBJ}}$ is derived with Eq. (16), and, from Eq. (14), the matrices of light codings REF and OBJ can be determined; (3) for known values of C_1, γ, REF, and OBJ, the estimate α_e of α is varied in Eq. (16), and the resulting matrix $\mathbf{D}_R$ is used as input in Eq. (17) to obtain height $\mathbf{z}_\alpha$. The height error $\Delta z_\alpha(j, k)/z(j, k)$ is then computed for each element of $\mathbf{z}_\alpha$. The dependence of $\Delta z_\alpha(j, k)/z(j, k)$ on $\Delta \alpha/\alpha$ is plotted in Fig. 6, with index j varied and index k kept constant; a variation of $\Delta \alpha/\alpha$ within the interval -40%–40% is supposed. It is evident that error $\Delta z_\alpha(j, k)/z(j, k)$ increases with $\Delta \alpha/\alpha$, and, the higher j, the higher the influence of $\Delta \alpha/\alpha$ on $\Delta z_\alpha(j, k)/z(j, k)$. In the experimental practice, this kind of error determines that, even for flat objects, the height profile measured in correspondence to points parallel to X

shows a slope with X. However, this effect can be canceled if $\Delta \alpha/\alpha$ equals zero.

4. Procedure for the Calibration of the System

The analysis performed so far allows us to develop a procedure to calibrate the system, aimed at finely adjusting the estimates of the system parameters until the required accuracy for the measurement is achieved. The control parameters are L and α. Parameter d is evaluated to the required accuracy during the setup phase and is not involved in the calibration. This choice is motivated by the fact that the sensitivity of the curve in Fig. 4 is twice as high as that in Fig. 5 and presents the opposite sign: thus, by finely varying the estimate of parameter L, we can even compensate for any influence of errors that is due to the estimate of parameter d.

Based on these observations, the calibration procedure estimates for angle α the value α_c, which minimizes Δz_α, and estimates for L the value L_c that minimizes the residual height error. The calibration master is a block of parallelepiped shape. The algorithm starts from the initial, rough estimates of L and α, denoted by L_0 and α_0, and is composed of two nested loops: The outer one evaluates L_c, and the inner one determines α_c.

At each iteration of the outer loop, the procedure calculates the profile of the master measured in correspondence to a section parallel to X. The exit condition is that the measured mean profile is within required accuracy δz. If this condition is not matched, the regression line is evaluated over the profile: if the angular coefficient is within a preset slope value, the current value α_e of angle α does not need any variation, and the procedure calculates a finer estimate L_e of L. We accomplish this by taking advantage of the linear dependence of the height on L in Eq. (17). Value L_e is then used to determine the profile of the master at the next iteration. If the exit condition is verified, current values L_e and α_e are assigned to the searched estimates L_c and α_c and the calibration stops; otherwise it enters the next iteration.

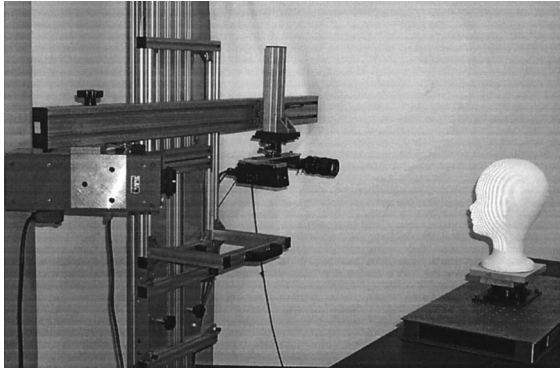The procedure enters the inner loop only if the

Fig. 7.   Photograph of the prototype used for the measurements.

Fig. 8.   Example of the GCPS sequence projected on the face model: shown are patterns (a) GC_0, (b) GC_3, (c) GC_7, (d) PS_1.

angular coefficient of the regression line evaluated over the master profile is greater than a preset value $\hat{m}$.   At each iteration, a new value for α_e is evaluated as

$$\alpha_e{}' = (1 + wm)\alpha_e, \qquad (26)$$

where $\alpha_e{}'$ and α_e are the new and the current values of α, respectively.   Parameter w is a weight factor, experimentally determined.   The resulting value of α_e is then used to evaluate a new profile for the master and the loop cycles until the exit condition is matched.

The algorithm converges very quickly: Typical values for the numbers of iteration are in the range 15–30.

5. Experimental Results

Figure 7 shows a photograph of the prototype used for the measurements.   The projector is based on a liquid-crystal panel (Model ABW LCD 320):   It projects fringes of rectangular profile, variable in contrast and frequency, and gray-code sequences; the video camera is a Sony XC-77CE, equipped with the CCTV Manual Iris (12.5–75-mm) zoom.   The acquisition and the elaboration of the images are performed by the PC Image MATRIX VISION framegrabber, with resolution $N = 800$ and $M = 2621$.

An extensive set of measurements has been performed to evaluate the overall performances of the system and to test the effectiveness of the calibration procedure.   In these experiments, the system has been calibrated having set as input to the calibration algorithm a value of height accuracy $\delta_z = 0.025$ mm and the value of parameter $\hat{m}$ used to determine α_c is $\hat{m} = 0.0001$.   The initial rough values for distance L and for angle α are $L_0 = 1080$ mm and $\alpha_0 = 0.4871$ rad.   The values determined by the calibration procedure after 16 iterations are $L_c = 1022$ mm and $\alpha_c = 0.332$ rad.

The first test refers to the face model shown in Fig. 7.   In this experiment, the field of view is 500 mm $\times$ 500 mm and the height range is 150 mm.   Figure 8 presents the deformation induced by the object shape on patterns GC_0, GC_3, GC_7, and PS_0 of the GCPS projection sequence; the 3D shape obtained by
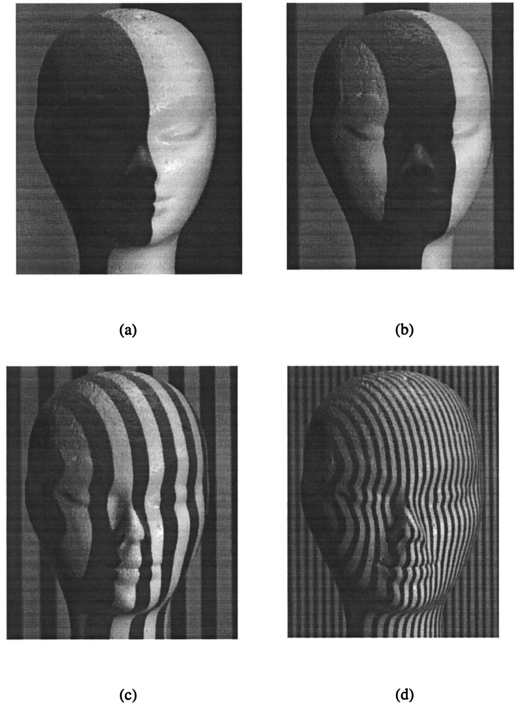
elaborating the complete pattern sequence is shown in Fig. 9.   It is quite evident that the system is able to detect both the height-slope changes of the nose as well as the local deformation that is due to the material used to build the model (polystyrene) in the forehead region.

The second example refers to the flowerpot in Fig. 10:   The presence of decorations on its surface makes this object particularly interesting to evaluate the resolution improvement achieved with the GCPS approach with respect to the gray code.   In fact, the ability of GCPS to detect the fine details on the surface can be clearly appreciated from Fig. 11(a):   In this case a resolution of 70 µm has been estimated. The same surface has been recovered by means of the gray-code technique: Fig. 11(b) shows a strong deg-

Fig. 9.   3D shape of the face model.

Fig. 10.   Image of a flowerpot.

Fig. 12.   In–out characteristic curves of the system.

radation of the measurement resolution, which has been calculated to be equal to 900 μm.

The In–out characteristic curves of the system that correspond to a number of test points on reference R have been also evaluated. To this aim, a plane has been used as a target object. It has been oriented parallel to reference R and moved along Z by means of a translation stage. A range of 80 mm, at steps of 4 mm each, has been considered. At each input position Z_{in}, the height Z_{out} of the target with respect to the reference has been measured as mean value over a set of 30 measurements. Figure 12 plots the in–out characteristic curves of the system derived in correspondence to a number of test points on plane R chosen at fixed Y, approximately at half of the illuminated area. All these curves are well approximated by lines: The angular coefficients evaluated over them are equal to 1 ± 0.0001 and show no de-

pendence on the X coordinate. This result highlights the good performance of the calibration, as the height error that is due to inaccuracy $\Delta\alpha/\alpha$ is compensated for.
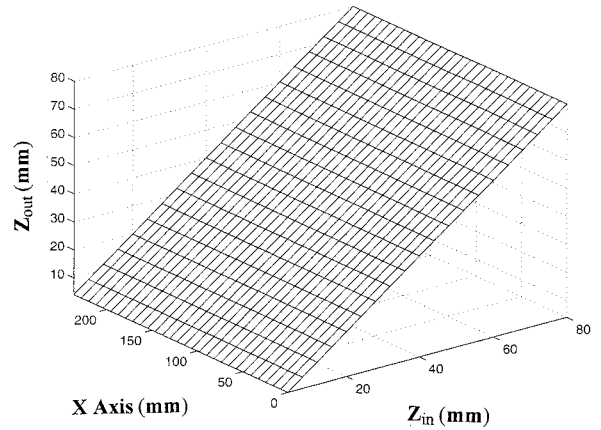
The dependence of the measurement error Δz versus Z_{in} has also been considered. To this aim, we evaluated the mean value $\overline{\Delta z}$ and the standard deviation $\sigma[\Delta z]$ of the distribution of error $\Delta z = z - Z_{in}$, where z is the height measured in correspondence to the same test points as before. Figure 13 plots the result: Both mean value $\overline{\Delta z}$ and standard deviation $\sigma[\Delta z]$ are shown as functions of Z_{in}. This figure well demonstrates the ability of the calibration to restrict the measurement error within a range of 12–33 μm, with a variability of ± 37 μm. The system characterization presented so far has been extended to a number of different sets of test points, taken in correspondence to sections parallel to X, at fixed values of Y. The analysis performed demonstrates that all the parameters presented so far, with the exception of the measurement dispersion, do not appreciably change with either X or Y. However, the mean square error $\sigma[\Delta z]$ increases by $\sim 70\%$ at the boundaries of the illuminated area: This is by no means surprising, considering that in these regions the quality of the fringes projected decreases, in both focus and contrast, and the influence of lens distortion increases.

(a)

(b)

Fig. 11.   3D shape of the flowerpot recovered with (a) the gray-code technique, (b) the combined GCPS technique.
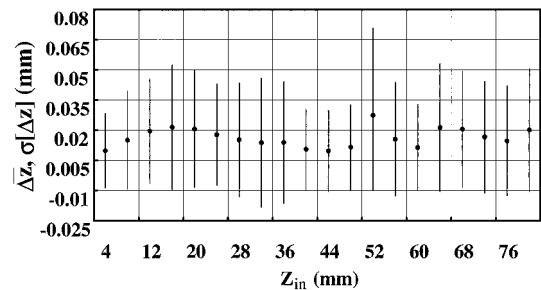

Fig. 13.   Evaluation of the accuracy of the system. The mean value $\overline{\Delta z}$ and standard deviation $\sigma[\Delta z]$ of the set of values of error Δz along a section parallel to X- are shown as functions of Z_{in}.

6. Conclusions

In this paper, a technique that combines the gray-code with the phase-shift methods into a whole-field profilometer has been presented. The resulting method, called GCPS, strongly improves the measurement performance in relation to resolution and range of measurement. It has been revised to compensate for the spatial modulation that the fringes present at the reference surface because of the crossed-optical-axes geometry of the system.

The analysis of the systematic errors and the procedure to calibrate the measurement profilometer based on the projection of structured light have also been presented. The calibration allows the evaluation of fine estimates of the geometric parameters of the system following a simple and non-time-crunching approach. An extensive set of measurements has been carried out to evaluate the measurement performance. The system shows high linearity and good performance as far as both accuracy and precision: The measurement error shows an overall mean value equal to 40 μm, with a variability of ±35 μm. The mean error can be further reduced by considering the lens distortion effects: A new model for both projector and video camera is under refinement and will be accounted for in future work.

References

1. F. Docchio, M. Bonardi, S. Lazzari, R. Rodella, and E. Zorzella, "Electro-optical sensors for mechanical applications," in *Optical Sensors and Microsystems*, A. N. Chester, S. Martellucci, and A. G. Mignani, eds. (Plenum, New York, London, 1999), Chap. 1.
2. S. F. El-Hakim and N. Pizzi, "Multicamera vision-based approach to flexible feature measurement for inspection and reverse engineering," Opt. Eng. **32,** 2201–2215 (1993).
3. D. Poussart and D. Laurendeau, "3-D sensing for industrial computer vision," in *Advances in Machine Vision*, J. L. C. Sanz, ed. (Springer-Verlag, New York, 1989), Chap. 3.
4. M. Rioux, G. Godin, F. Blais, and R. Baribeau, "High resolution digital 3D imaging of large structures," in *Three-Dimensional Image Capture*, R. N. Ellson and J. H. Nurre, eds., Proc. SPIE **3023,** 109–118 (1997).
5. R. A. Jarvis, "A perspective on range finding techniques for computer vision," IEEE Trans. Pattern Anal. Mach. Intell. **PAMI-5,** 122–139 (1983).
6. S. Kuwamura and I. Yamaguchi, "Wavelength scanning profilometry for real-time surface shape measurement," Appl. Opt. **36,** 4473–4482 (1997).
7. T. Nielsen, F. Bormann, S. Wolbeck, H. Spiecker, M. D. Burrows, and P. Andersen, "Time-of-light analysis of flight pulses with a temporal resolution of 100ps," Rev. Sci. Instrum. **67,** 1721–1724 (1996).
8. M. Rioux, "Laser range finder based on synchronized scanners," Appl. Opt. **23,** 3837–3843 (1984).
9. Q. Fang, and S. Zheng, "Linearly coded profilometry," Appl. Opt. **36,** 2401–2407 (1997).
10. T. G. Stahs and F. M. Wahl, "Fast and robust range data acquisition in a low-cost environment," in *Close-Range Photogrammetry Meets Machine Vision*, E. P. Baltsavias and A. Gruen, eds., Proc. SPIE **1395,** 496–503 (1990).
11. G. Sansoni, S. Corini, S. Lazzari, R. Rodella, and F. Docchio, "Three-dimensional imaging based on Gray-code light projection: characterization of the measuring algorithm and development of a measuring system for industrial applications," Appl. Opt. **36,** 4463–4472 (1997).
12. G. Sansoni, S. Lazzari, S. Peli, and F. Docchio, "3D imager for dimensional gauging of industrial workpieces: state of the art of the development of a robust and versatile system," in *Proceedings of the International Conference on Recent Advances in 3-D Digital Imaging and Modeling*, G. Roth and M. Rioux, eds., (IEEE Computer Society, Los Alamitos, Calif., 1997), pp. 19–26.
13. W. Krattenthaler, K. J. Mayer, and H. P. Duwe, "3D-surface measurement with coded light approach," in *Fourth International Workshop for Digital Image Processing and Computer Graphics*, Proceedings of Österreichische Arbeitsgem. MustererKennung (ÖCG Schriftenreihe, Oldenburg, Germany, 1993), Vol. 12, pp. 103–114.
14. G. Sansoni, M. Carocci, S. Lazzari, and R. Rodella, "A 3D imaging system for industrial applications with improved flexibility and robustness," J. Opt. A **1,** 83–93 (1999).
15. M. Carocci, S. Lazzari, R. Rodella, and G. Sansoni, "3D range optical sensor: analysis of the measurement errors and development of procedures for their compensation," in *Three-Dimensional Image Capture and Applications*, R. N. Ellson and J. H. Nurre, eds., Proc. SPIE **3313,** 178–188 (1998).